The use of dimensionality reduction techniques for fault detection and diagnosis in a AHU unit: critical assessment of its reliability

Hugo Geoffroy, Julien Berger, Benoît Colange, Sylvain Lespinats, Denys Dutykh

The use of dimensionality reduction techniques for fault detection and diagnosis in a AHU unit: critical assessment of its reliability

Hugo Geoffroy[a], Julien Berger [b*], Benoît Colange[c], Sylvain Lespinats[c], Denys Dutykh[d]

November 8, 2022

[a] Univ. Grenoble Alpes, Univ. Savoie Mont Blanc, CNRS, LOCIE, 73000 Chambéry, France
[b] Laboratoire des Sciences de l'Ingénieur pour l'Environnement (LaSIE), UMR 7356 CNRS, La Rochelle Université, CNRS, 17000, La Rochelle, France
[c] Univ. Grenoble Alpes, INES, F-73375, Le Bourget du Lac, France
[d] Univ. Grenoble Alpes, Univ. Savoie Mont Blanc, CNRS, LAMA, 73000 Chambéry, France.

Abstract

Fault Detection and Diagnosis (FDD) are important tools to perform on-going monitoring of the systems and help in their building commissioning. An innovative method is investigated based on combined data-driven and knowledge-based approaches. This article presents the method. First phase, a so-called operating map of the system is built using dimension reduction method and numerical or experimental dataset. This map is composed of several regions corresponding to nominal operation and to specific faults. The second phase focuses on the FDD. The monitored data are projected on the map. According to the position, a clear and precise fault detection and diagnosis can be carried. The method is applied to an air handling unit. The map is built using data generated with a building simulation program. The reliability of the method is proven using experimental data of nominal and fault operation generated.

Key words: Fault detection and diagnosis; Heating Ventilation and Air-Conditionning systems; data-driven approach; knowledge-based approach; dimensionality reduction technique

1 Introduction

According to the United States Department of Energy, the building sector is the biggest consumer of primary energy in the USA amounting to 41 % of the total energy consumption [1, 2]. Among these huge energy uses, 50 % are directly consumed by the Heating, Ventilation and Air-Conditioning (HVAC) systems [3]. It is also known that the HVAC systems usually do not operate as required, causing supplementary energy consumption. A recent study showed that the HVAC operation problems can induce a waste between 25 % to 50 % of the consumed energy [4]. With a good follow-up, the energy consumption can be reduced by 15%. These HVAC operation problems can be caused by several different sources such as breakdown of components, efficiency drift or control problems. For these reasons, the control of HVAC systems in existing buildings is a major issue.

The building commissioning aims to respond to this issue with on-going monitoring among other approaches. Particularly, simple and automated Fault Detection and Diagnosis (FDD) are developed to help the maintenance staff to take care of the equipment in detecting the problems as fast as possible. Nowadays, the required characteristics for HVAC systems FDD are known. Venkatasubramanian listed the ten wanted criteria of a FDD system: quick detection and diagnosis, isolability, robustness, novelty identifiability, classification error estimate, adaptability, explanation facility, modeling requirement and multiple fault identifiability [5]. In a general way, they aim at detecting the occurrences of malfunctions during the equipment operation, to inform operation or maintenance staff in the shortest possible time to avoid violating indoors comfort or too high energy use.

The FDD techniques have been classified into four main branches for Air Handling Unit (AHU) [6–8]: analytical-based methods, knowledge-based methods, data-driven methods, and a combination of all of those. The first approach compares measured data to simulated ones obtained from mathematical model. The fault detection in systems is realized by computing the residual. One of the main advantages is to detect

unknown faults without huge quantity of measured data. Nevertheless, numerical models may be complex and face computational issues. The knowledge-based approaches use expert analysis to extract rules from data and detect faults. No model are required but usually unknown faults are not detected. The data-driven methods search for relations among data patterns and identified faults. It does not need any complex model or expert information, even unknown, but the capacity to diagnose can be reduced. Combination of these different methods appeared in recent years to solve the inherent problems of individual techniques.

Since the creation of the "Annex 25" of the International Energy Agency (IEA) developed in the frame of the Energy Conservation in Buildings and Community Systems (ECBCS) in 1999 [9], the real implementation of these tools in buildings areas remains an important issue. Indeed, it is still an open challenge for real time FDD tools to present the results in a clear and intelligible form. It requires to be understandable to all maintenance operators regardless of their qualification to analyze the FDD tools outputs [10]. Furthermore, with the development of smart buildings, a new challenge appears [11]. There is a big amount of data to deal with, and old methods are not always able to cope with it. Indeed, even in residential areas, it may produce a huge amount of data for regulation of the simplest systems, as Air Handling Unit (AHU) with numerous measured data recorded at short time steps. This context increases the computing time and makes the FDD complex or too expensive for residential buildings. As mentioned in [12, 13], the energy management systems lack in consolidating the data into a clear and understandable format by operators.

Thus, the aim of this article is to explore a new fault detection and diagnosis method for the building area. It is based on a combination of data-driven and knowledge-based approaches. This combination intends to produce *one* information easily understandable by operators to detect nominal and faulty operation of the system. The method is separated in two phases. The first one aims at creating a so-called operating map of the system using a dimension reduction method and a set of data. The latter can be generated from an experimental campaign and/or a numerical model. The dimension reduction method enables to reduce the high dimensional space of indicators into a lower two-dimensional representation. Such map is composed of several regions corresponding to the nominal operation and to specific faults. The second phase aims at following the system operation. For this, the monitored data of the system are projected on the map. Depending on the position, a clear and easy detection and diagnosis of the fault can be performed.

The structure of the article is as follows. Next Section presents the methodology with emphasis on the offline and online phases. Then, in Section 3 is applied to an AHU unit. The map is generated using a building simulation program. The reliability of the method is evaluated using experimental data obtained from a campaign detailed in [14]. Some conclusions are made in Section 4.

2 Methodology

The data-driven and knowledge-based methods are now presented. Two phases are distinguished: *(i)* the offline phase that enables to create a map of the system operation and *(ii)* the online phase when the fault detection and diagnosis is carried out.

2.1 Offline phase: map construction

2.1.1 Data filtering

The first step of the method consists in treating the data regarding the operation rules. It enables to create the so-called input data space. The so-called input data arises from two possible sources: *(i)* numerical synthetic data generated with a building simulation programs or *(ii)* measured data obtained from building energy management systems. Usual data are temperature, electrical power, airflow rated or logical values. Let's denote by N_m the number of input data, obtained on a time grid $\{ t_n \}, n \in \{ 1, \dots, N_t \}$. Note that N_t is the total number of time acquisitions. The original dataset is defined by:

$$U \stackrel{\text{def}}{:=} \{ \boldsymbol{U}_n \}, \quad n \in \{ 1, \dots, N_t \}, \tag{1}$$

where $\boldsymbol{U}_n \in \mathbb{R}^{N_m}$ is a vector composed of the N_m input quantities at the time instant t_n:

$$\boldsymbol{U}_n \overset{\text{def}}{:=} \Big(U_1(t^n), \dots, U_{N_m}(t^n) \Big) \;=\; \Big(U_i(t^n) \Big), \quad i \in \{1, \dots, N_m\}. \tag{2}$$

The treatment is carried out according to the operation rules defined by the user for the fault detection. A rule represents logical statements observed in a regular operation of the building. It is defined, at each time instant t^n:

$$U_i(t^n) \;-\; U_j(t^n) \;=\; U_\infty, \quad (i, j) \in \{1, \dots, N_m\}^2, \quad i \neq j, \tag{3}$$

where U_∞ is a chosen limit value so that, by convention, a fault is detected when

$$U_i(t^n) \;-\; U_j(t^n) \geqslant U_\infty. \tag{4}$$

A total of N_R rules are created and gathered in the following set:

$$\rho \overset{\text{def}}{:=} \{ \boldsymbol{\rho}_n \}, \quad n \in \{1, \dots, N_t\}, \tag{5}$$

with $\boldsymbol{\rho}_n \in \mathbb{R}^{N_R}$ is a vector composed of the N_R rules:

$$\boldsymbol{\rho}_n \overset{\text{def}}{:=} \Big(\rho_1(t^n), \dots, \rho_{N_R}(t^n) \Big) \;=\; \Big(\rho_k(t^n) \Big), \quad k \in \{1, \dots, N_R\}. \tag{6}$$

The element $\rho_k(t^n)$ is a so-called expert rule, where the results of logic rules are treated in a dimensionless form:

$$\rho_k(t^n) \overset{\text{def}}{:=} \frac{U_{i_k}(t^n) \;-\; U_{j_k}(t^n) \;-\; U_{\infty_k}}{\beta_k}, \quad (i_k, j_k) \in \{1, \dots, N_m\}^2, i_k \neq j_k, \tag{7}$$

The factor β is used as a gravity indicator to the fault detection process. Note that a rule can be composed of several sub-rules that are combined using logical inclusions. The result of the expert rules are then processed with an hyperbolic tangent function to create the severity index (SI) denoted by σ and computed according to:

$$\sigma \overset{\text{def}}{:=} \{ \boldsymbol{\sigma}_n \}, \quad n \in \{1, \dots, N_t\}, \tag{8}$$

where $\boldsymbol{\sigma}_n \in \mathbb{R}^{N_R}$ is a vector composed of the N_R severity indices:

$$\boldsymbol{\sigma}_n \overset{\text{def}}{:=} \Big(\sigma_1(t^n), \dots, \sigma_{N_R}(t^n) \Big) \;=\; \Big(\sigma_k(t^n) \Big), \quad k \in \{1, \dots, N_R\}, \tag{9}$$

and

$$\sigma_k(t^n) \overset{\text{def}}{:=} \tanh\Big(\rho_k(t^n) \Big). \tag{10}$$

Thus, the severity index presents a dimensionless indicator in the range $]-1, 1[$, regardless of the nature of the fault or the data. At the time t^n, a negative value $\sigma_k(t^n) < 0$, indicates a nominal function of the system regarding the rule k. Contrarily, a positive value $\sigma_k(t^n) > 0$, stands for a faulty operation. As illustrated in Figure 2(a), the quantity β guides the transition between the nominal and faulty state. This transformation also enables to compare the indicators among them.

Another indicator is created to detect the emergence of multiple faults. The total fault severity is denoted by λ and defined as follows:

$$\lambda \overset{\text{def}}{:=} \{ \lambda_n \}, \quad n \in \{1, \dots, N_t\}, \tag{11}$$

where

$$\lambda_n \overset{\text{def}}{:=} \sum_{k=1}^{N_R} {\sigma_k}^+ (t^n), \qquad {\sigma_k}^+ \overset{\text{def}}{:=} \max(\sigma_k, 0). \tag{12}$$

Thus, ${\sigma_k}^+$ corresponds to the positive part of the severity index, indicating the appearance of a fault. The last indicator corresponds to the total number of faults appearing simultaneously:

$$\delta \overset{\text{def}}{:=} \{ \delta_n \}, \quad n \in \{ 1, \dots, N_t \}, \tag{13}$$

with

$$\delta_n \overset{\text{def}}{:=} \sum_{k=1}^{N_R} \chi_{[0,1]}\Big(\sigma_k(t^n) \Big), \tag{14}$$

where $\chi_{[0,1]}(\bullet)$ denotes the indicator function of the subset $[0, 1]$.

2.1.2 Construction of two-dimensional maps of the system state using manifold learning

As mentioned above, the set σ includes all the severity indices representing the state of the system. However, this matrix describes data in a high dimensional space. Typically, N_t scales with $\mathcal{O}(10^4)$. For the number of rules N_R, it range depends on the complexity of the system and varies between $\mathcal{O}(10)$ and $\mathcal{O}(10^2)$. Dimension reduction techniques are used to embed the input points, associated to the set σ, into a subspace of lower dimensionality. Here the dimension of the subspace is two to enable an easy and comprehensive visual representation of the system state. Such representation is referred to as a map. The procedure is carried out as follows. First, to reduce the computational cost, a subset of the N_H most representative points is obtained using a clustering method [15] and selecting the prototypes of each cluster. This algorithm identifies the clusters minimizing the cumulated distance separating each point from the prototype of its cluster. Hence, the selected points provide a good representation of the dataset dispersion in the original space.

Then, several dimensionality reduction techniques can be employed. The general goal of this mapping methods is to embed the dataset lying in the original high dimensional space onto a low dimensional output space while preserving as much as possible the data structure. In that framework each item originally described by many coordinates in the original space is positioned with a few coordinates in the output space. The Principal Component Analysis (PCA) [16] is one of the best-known dimension reduction technique, performing the linear projection of data that preserves the most of the data variance. The classical multidimensional scaling method [17] is another well-known approach based on distance metrics. Yet, those approaches are not suited for data that lie on a non-linear manifold of the space. Thus, we choose to focus here on methods which are designed for such data and focus on the preservation of the neighbourhoods of each point. These methods derived from Stochastic Neighbor Embedding (SNE) [18] also include tSNE [19], NeRV [20], JSE [21], etc) try to preserve the neighbourhoods ranks. A high number of techniques are described in the literature; a review may for example be found in [22].

Practically, the dimensionality reduction enables to represent data from a high dimensional space onto a space of lower dimensionality (dimension two) called map. An illustration of this approach is shown in Figure 1. The original data in the three dimensional space (S-shaped surface) can be represented into a two-dimensional one, using different methods. All these methods attempt to preserve the structure of the data. Indeed, the original spatial organization of points is conveyed by the maps, as shown by the reproduction of the red, yellow, blue color gradient along the surface.

There is no classification of faults regarding their degree of severity with the dimensionality reduction. In other words, there is no information that the red dots is more important than the blue ones when considering Figure 1. The key point of the reduction is to maintain the red (and others) dots in a same region in the reduced space. The approach helps the user to decide if the system is in a faulty or nominal state (defined by the expert rules). It does not provide any classification or hierarchy of the states. If the user considers the red dots as a strong important fault, then *they* should decide to operate on the system.

In the present paper, we use ASKI [24]. Indeed, tSNE tends to show a more desirable than SNE for very high dimensional data but the opposite phenomenon is observable in case of low dimensional space. ASKI adapts its kernel to the intrinsic dimension of the input data leading to a behaviour more robust to the data

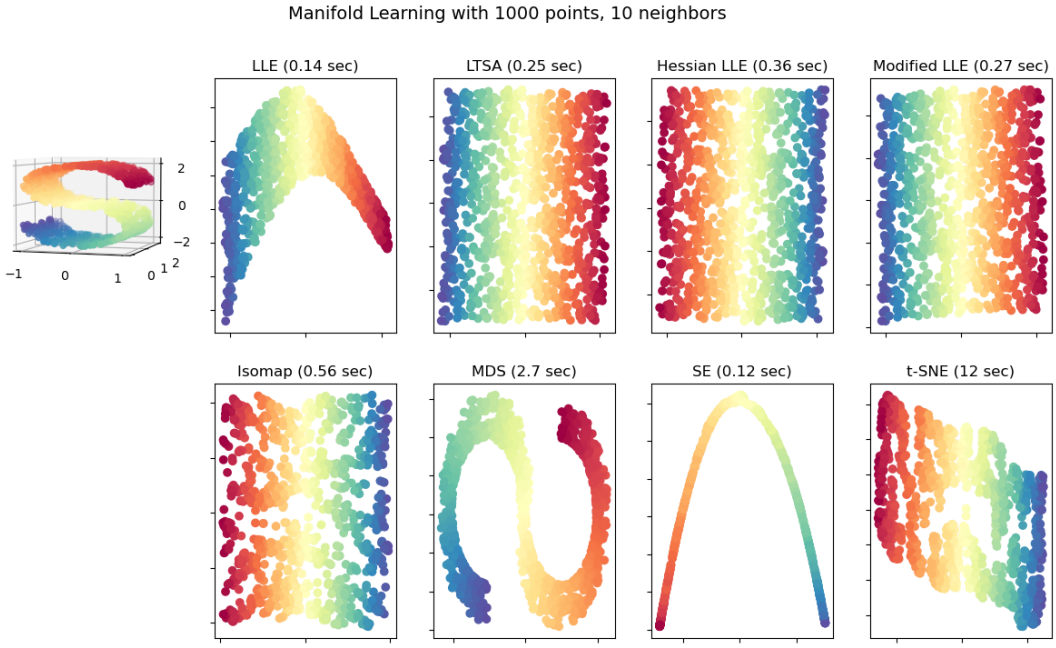

Figure 1. *Example of dimensionality reduction taken from [23]. The insert in the left of the Figure shows the input data in the original 3D space. The points color depends on the position along the 2D sub-variety on which data lie. The organization of data is expected to be preserved while mapped onto 2D spaces according to various multidimensional scaling methods. Eight maps reached by eight different mapping methods are drawn in other inserts. We can observe that the structure (which is consistent with color) is often preserved.*

dimension. The method maps the severity indices selected using the HASTIE's sampling algorithm [15]:

$$f \,:\, \mathcal{M}at\,(\,]-1\,,\,1\,[\,,\,N_t\,,\,N_R\,) \longrightarrow \mathcal{M}at\,(\,\mathbb{R}\,,\,N_H\,,\,N_D\,)\,, \tag{15}$$

$$\sigma \longmapsto \widetilde{\sigma}\,, \tag{16}$$

where N_H is the number of points selected by the HASTIE method and N_D is the dimension of the subspace. In the end, the offline phase allows an easily understandable representation of the input data composed of quantities with physical dimensions through a space of reduced size. Since in this work $N_D = 2$, the reduced space is identified as a map.

In order to obtain a map of the data, ASKI relies on the minimization of a stress function whose variables are the position of points in the map. This stress function assesses, for any given map of the data that may be considered during the optimization process, the level of distortion of the data structure associated to this map. The preservation of the data structure is measured by comparing between the data space and the map, the rate of belonging of each point j to the neighbourhood of each point i. In the data space, these belonging rates are given by:

$$\beta_{ij} \overset{\text{def}}{:=} \frac{\left(1+\frac{\Delta_{ij}^2}{\lambda_i\sigma_i^2}\right)^{-\frac{\lambda_i+1}{2}}}{\sum_{k\neq i}\left(1+\frac{\Delta_{ik}^2}{\lambda_i\sigma_i^2}\right)^{-\frac{\lambda_i+1}{2}}}, \tag{17}$$

while in the map, they are expressed as:

$$b_{ij} \overset{\text{def}}{:=} \frac{\left(1+\frac{D_{ij}^2}{ls_i^2}\right)^{-\frac{l+1}{2}}}{\sum_{k\neq i}\left(1+\frac{D_{ik}^2}{ls_i^2}\right)^{-\frac{l+1}{2}}}, \tag{18}$$

where Δ_{ij} and D_{ij} are the distances between point i and j in the data space and map respectively. Parameters σ_i and s_i are scaling factors, where σ_i is set by the perplexity as defined in [18], while λ_i and l are the degrees of freedom of the Student kernels defined as the intrinsic dimensionality of data and as the embedding space dimensionality respectively. The stress function ζ is then computed by comparing the distribution of belonging rates between the two spaces with a mixture of Kullback–Leibler divergence:

$$\zeta \overset{\text{def}}{:=} \sum_i \sum_{j\neq i} \beta_{ij} \log\left(\frac{\beta_{ij}}{b_{ij}}\right) + b_{ij}\log\left(\frac{b_{ij}}{\beta_{ij}}\right). \tag{19}$$

The map is then optimized to minimize the function ζ.

2.2 Online phase: projection on the maps

During the second phase, measured data monitored by the building energy management system are obtained. The purpose of the FDD tool is to analyze such data to evaluate if the system is working in its nominal or faulty state. To do so, first the measured data are filtered according to the same methodology presented in Section 2.1.1. As mentioned before, this step is essential to obtain dimensionless quantities that can be compared to each other. Let's denote by $\boldsymbol{\sigma}' \in \mathbb{R}^{N_R}$ the new N_R severity indices obtained from measured data at a given time instant. Then, those indices are projected on the reduced space using Radial Basis Functions (RBF) according to:

$$\widetilde{\boldsymbol{\sigma}'} = \sum_{n=1}^{N_t} \lambda_n \, \phi\Big(||\, \boldsymbol{\sigma}' - \boldsymbol{\sigma}_n \,|| \Big), \tag{20}$$

where ϕ is a kernel function and $\{\lambda_n\} \in \mathbb{R}^N$ are some real coefficients. In our computations, a Matern RBF kernel is employed. It is important to underline that the computation of the coefficients $\{\lambda_n\}$ is performed during the *offline* procedure, to reduce the computational cost of the online phase. Then, during the online phase, the numerical complexity of the map scales with $N_R \times N_H$ only, which is very satisfying. The computational cost of the projection is low so that real time prediction can be performed.

2.3 Synthesis

As a synthesis of the general methodology, a diagram of mapping is illustrated in Figure 2(b) for the offline and online processes, respectively. For the offline process, given the input data, the expert rules enables to define the severity indices. Then, the Hastie algorithm is used to select N_H points. From the manifold $N_H \times N_t$, the dimensionality reduction technique enables to generate a lower subspace of dimension $N_D \times N_t$. For the online process, at each time instant, the measured data are treated according the expert rules. Then, a projection is carried out from $\mathbb{R}^{N_R}$ to $\mathbb{R}^2$, so the severity index of the measured data can be positioned in the subspace.

The Algorithm 1 gives the main steps of the FDD approach. The offline phase includes two programming parts. First, the data filtering can be implemented with several programming language/environment such as `Python`, `Matlab`, `C++` or even `VBA/Excel`. There is no existing toolbox for this part but it should be very accessible (basic sum, minus and tangent operations). Then, for the dimensionality reduction, several tools are available in the literature, mainly in `Python` and `Matlab` environments. For the primer (`Python`), the `Scikit-learn` package can be employed [25]. For the latter (`Matlab`), the dimensionality reduction toolbox developed L. Van der Maaten and co-workers (available at https://lvdmaaten.github.io/drtoolbox/)

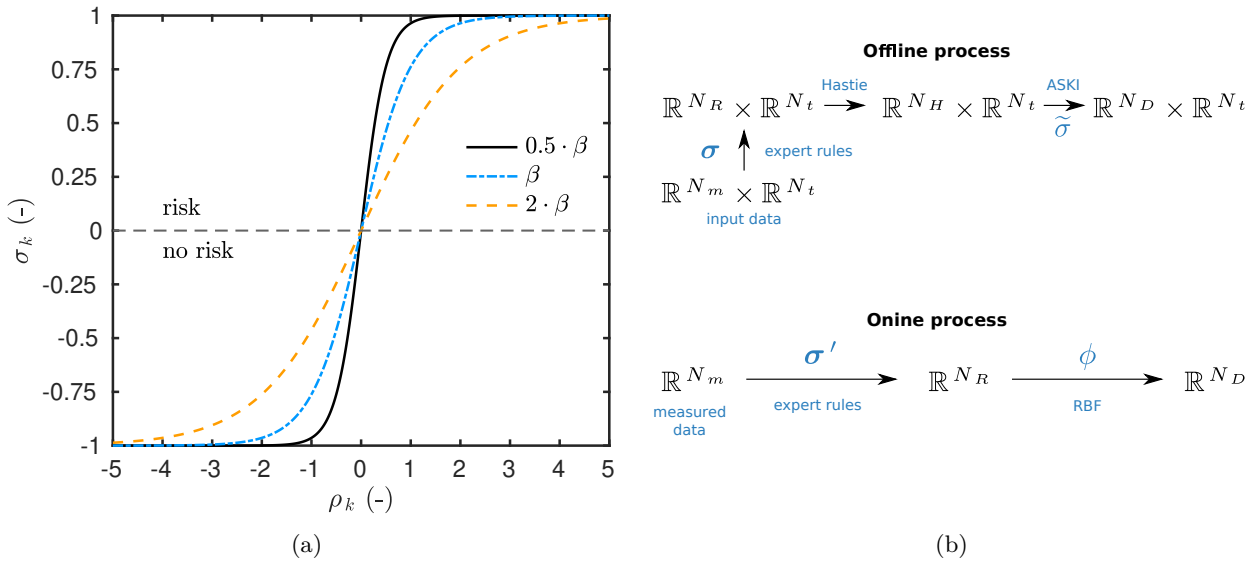

(a) (b)

Figure 2. (a) *Illustration of the severity index and the influence of the parameter* β *.* (b) *Diagram of mapping of the offline and online processes.*

proposes many algorithms with a lot of practical examples for implementations. However, in the paper, the ASKI method (thoroughly described in [24]) has been used for its interesting properties according to the specific task. A shared `Matlab` code for ASKI is available as open source code on the code ocean platform [26].

Regarding the online phase, the filtering of the measured data can be carried out by the same code implemented previously. The projection on the map using RBF function can be easily programmed in the same environments (`Python`, `Matlab`, `C++` or even `VBA/Excel`). Nowadays it is already included in several packages of `Python` (`Scipy`) or `Matlab` toolboxes (Mathworks community and more precisely `dace toolbox` [27]) environments.

Algorithm 1 Basic steps of the data-driven and knowledge-based FDD algorithm.

▷ *Offline phase: data filtering* (Self programming)
Generate numerical data $\boldsymbol{U}$ using `EnergyPlus`;
Define & compute the expert rule associated using Eq. (7);
Compute the severity indices associated using Eq.(10);
▷ *Off-line phase: build 2D map* (`ASKI` package [26])
Select N_H most representative points;
Create map of the system operations using ASKI approach ;
Compute coefficients of RBF basis in Eq. (20);
▷ *Online phase: projection on the maps* (Self programming)
Record experimental data $\boldsymbol{U}'$ from building energy management system;
Compute the expert rule associated using Eq. (7) ;
Compute the severity indices $\boldsymbol{\sigma}'$ associated using RBF Eq. (20);
Place coordinate $\widetilde{\boldsymbol{\sigma}}$ on the map;
Operator establishes diagnosis by reading the map;

Regarding the practical implementation of the method in real buildings, the off-line phase consists in elaborating the map using existing monitored data or numerical data generated with a simulation program. The data are then treated using expert rules and multi-dimensional scaling. The former can be easily program while the latter can be carried using the above-mentioned programming packages. This step should be carried by engineers in charge of the design of the HVAC system (in collaboration with operators). Indeed,

it requires to define the expert rules and then to program them. At the end of this phase, a map of the system operation is produced. The engineer needs to implement it on the building management system. Then, during the on-line phase, the faulty and nominal operations are followed. It can be achieved by maintenance operators. It consists in reading the map and checking if the projected points of the actual measurements are located in nominal or faulty areas. All information are gathered into one single map. No programming skills are required by the operators. One or two times per year, the engineers can interacts by updating the map with new experts rules and experimental data if needed.

3 Case study

3.1 Offline phase: maps construction using a building simulation program

3.1.1 Input data simulation

To build the map of the system operation, a building simulation program is used to generate the so-called input data. As in a authentic engineering situation, the `EnergyPlus` software is employed to model a small office building inspired from a real case. Such building could use the ventilation system described in [14]. For the simulations, the building is located in Bordeaux, France, so that standard climate is used. There is no shadings induced by the urban surroundings. The surface is 200 m^2 split in two storeys. The general plan of the building is given in Figure 3(a). The first 160 m^2 floor is composed of two thermal zones: the offices zone and a reception zone, which includes archives, xerography, waiting room and reception. The second floor represents the third thermal zone with a private meeting room of 40 m^2. An illustration of the main North-oriented facade is shown in Figure 3(b), based on the `Sketchup` software. The enclosures of the building have a global thermal resistance of 4.85 $\mathsf{m}^2.\mathsf{K}.\mathsf{m}^{-1}$, 4.15 $\mathsf{m}^2.\mathsf{K}.\mathsf{m}^{-1}$ and 9 $\mathsf{m}^2.\mathsf{K}.\mathsf{m}^{-1}$, for the vertical surfaces, the terrace floor and the flat roof, respectively. According to the regulations, each office has an air change rate of 25 $\mathsf{m}^3.\mathsf{h}^{-1}$. For the meeting and welcome zones, it equals to 30 $\mathsf{m}^3.\mathsf{h}^{-1}$ and 182 $\mathsf{m}^3.\mathsf{h}^{-1}$, respectively. The global air change rate is 0.49. The building occupancy is from 8 $a.m.$ to 8 $p.m.$ from Monday to Friday, with a reduced rate for the Saturday. Standards heat generation due to occupants, lights and systems is included in the simulation.

Concerning the HVAC systems, the inside temperature is regulated by an Air Handling Unit (AHU) combined with radiant panels in each room. The AHU used is the same as the one presented in [14] and a schematic representation is shown in Figure 4. The system is modeled in `EnergyPlus`. The demand side corresponds to the loads (in case of cooling) or demand (in case of heating). It includes the different thermal zones and networks. The supply side comprises the components for air treatment and movement. The frost coil belongs to this part. Its set-up temperature is set to 5 $\mathsf{°C}$. Next to heating air exchanger, a mixturing component has been included in the modeling that does not exist in the system presented in [14]. It is imposed by the software. However, it should not affect the results since the mixture rate is set to 0 %. The blow in air branch is divided in three sub-branches connected to each of the three thermal zones.

To generate the input data, nominal and faulty operation of the building are simulated. A total of 19 failures cases are modeled based on two complementary simulations (one for each season). According to the definition given in [14, Section 2.5.2], 6 global faults, 4 winter faults and 3 summer faults are generated. The global faults includes: supply and exhaust fans failures, fans belts breakdown and filter fouling. For the winter, there are heating/frost coils failures, heating/frost coils regulation problems and simultaneous failure of both coils. For winter, the faults arise from three regulation problems of free cooling. Note that fan failures occurs for supply, exhaust or both of fans. A synthesis of the failure is presented in Figure 5. The results of the simulations are obtained for a time step of 15 min, using two annual simulations (one for winter and one summer faults), so the number of acquisition is $N_t = 70080$. A total of $N_m = 12$ simulated input quantities are extracted from those results. Thus, the total number of input data is $N = N_t \cdot N_m$.

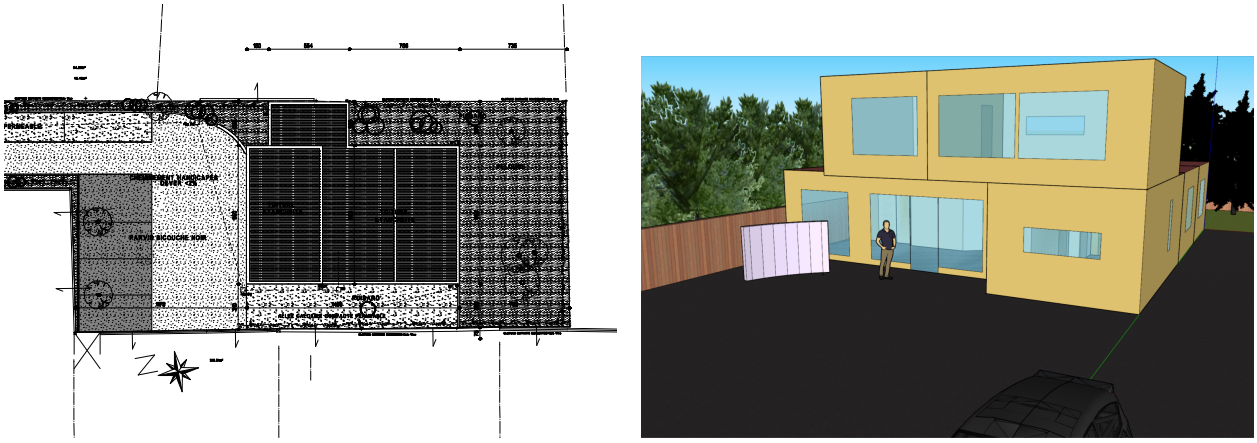

(a) (b)

Figure 3. *General plan* (a) *and main North-oriented facade* (b) *of the building*

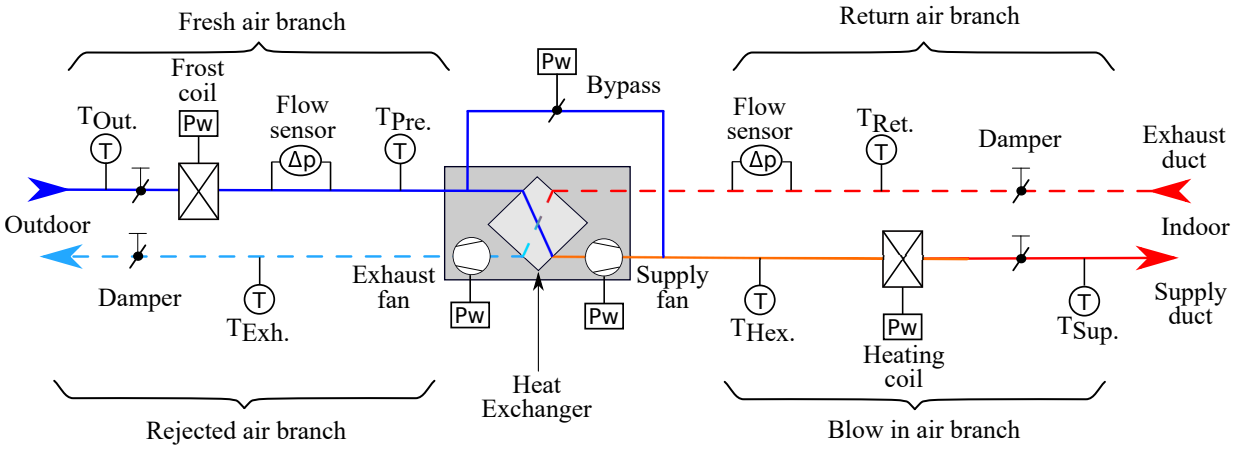

Figure 4. *Schematic representation of the AHU system with the interested measured quantities.*

3.1.2 Expert rules

The input data are first filtered using the expert rules. For the winter season, eight rules are defined as reported in Table 1. The formalism of Eq. (7) is employed with the coefficient values given in the same Table. Each rule is composed of at least two sub-rules. The rule ρ_1 represents a supply fan failure. It is highlighted by two sub-rules: one analyzing if the airflow decreases to a null value and one verifying if the electrical power is lower than a user-defined value. Similar logic applied to the exhaust fan is adopted for the rule ρ_2. The third rule is for the frost coil failure. It occurs when the electrical power of the component is turned off while the outside temperature does require to pre-heat the entering air $T_{out} < 5$ °C. Similar logic applied to the heat coil is used for rule ρ_4. Here, the regulation fault appears when the temperature difference between the supply air and the set-point is higher than one degree: $T_{c,sup} - T_{sup} > 1$ °C. Note that the set-point temperature of the heat coil is set to $T_{c,sup} = 26$ °C. The exhaust fan belt breakdown is represented by ρ_5 and two sub-rules. The first one checks if airflow rate is almost null. The second analyses if the electrical consumption of the fan is still positive (at a value probably lower than the nominal one). For the frost coil regulation faults, four sub-rules are needed. The first one verifies if pre-heating is required using the outside temperature. The next one looks if the battery is turned on using its electrical consumption. The third sub-rules confirm that the fan is working. Last, instabilities in the temperature are detected. For the latter, the field of interest is the time derivative of the pre-heating temperature denoted

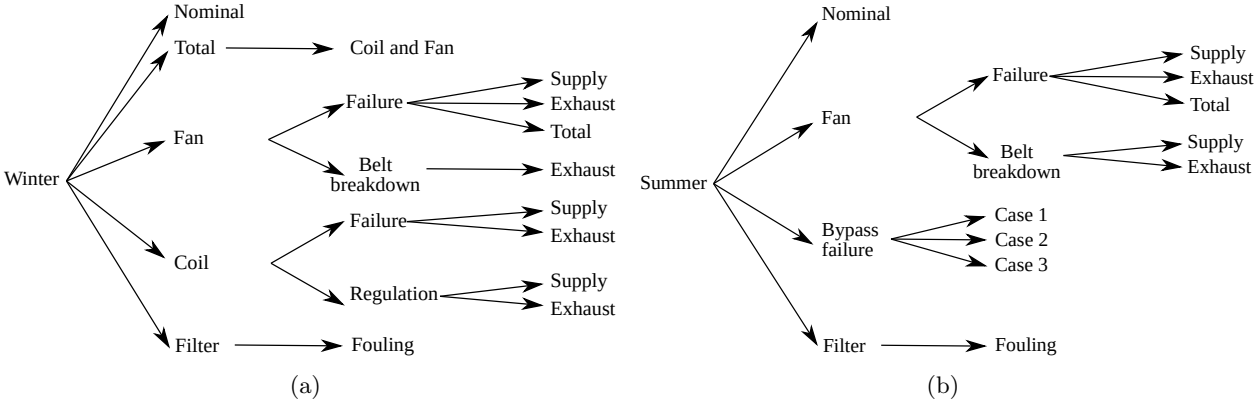

Figure 5. *Synthesis of the failure and nominal cases generated with building simulation program for summer* (a) *and winter* (b).

by T'_{pre}. It is computed using a second order backward finite-differences approximation:

$$T'_{pre}(t^n) \stackrel{\text{def}}{:=} \left| \frac{T_{pre}(t^n - 2\cdot\Delta t) - 2\cdot T_{pre}(t^n - \Delta t) + 3\cdot T_{pre}(t^n)}{2\cdot\Delta t} \right|, \tag{21}$$

where Δt is the time step between two input data. The default appears when $T'_{pre} > 0.1$ indicating fluctuation of the pre-heating temperature. The same approach is extended for the seventh rule. The quantity T'_{sup} is defined following Eq. (21). Note that sub-rules $\rho_{3.2}$, $\rho_{6.1}$ and $\rho_{7.1}$ are equal and sub-rule $\rho_{3.1}$ is opposite to $\rho_{6.2}$ and $\rho_{7.2}$. The last fault concerns the filter fouling. It happens when the fan airflow operates in nominal conditions ($Q_{v,sup} > -0.103\ \mathsf{kg.s^{-1}}$) and when the supply fan power is higher than nominal conditions, with a threshold defined at 40 W.

For the summer period, eight expert rules are defined with associated coefficients reported in Table 2. The rules ρ_1, ρ_2 and ρ_8 are equivalent to their counterparts for winter season. The rule ρ_3 is the same as ρ_5 for winter season. And ρ_4 is the extension of ρ_3 for the supply fan. Rules 5 to 7 concern failure in the bypass regulation in the framework of free-cooling. It is recalled that free-cooling occurs in summer period when the outside temperature is lower than inside one. Thus, the bypass of the AHU should be turned on to avoid the heat exchanger and in the same time, the airflow rate should be increased. The rule ρ_5 occurs when neither the bypass is not turned on and the airflow rate is not increased. To identify such fault, four sub-rules are required. The first one detects a period when free-cooling is favorable. It is based on a moving average over three values for the outside $\overline{T}_{out}$ and inside $\overline{T}_{ret}$ temperatures. Free-cooling should happen when $\overline{T}_{ret} - \overline{T}_{out} > 2\ ^\circ\mathsf{C}$. Second sub-rule $\rho_{5.2}$ looks at the state of the bypass b. Sub-rule $\rho_{5.3}$ checks if the value of the moving average flow rate $\overline{Q}_{exh}$ is in the range of 10% of its nominal value at low speed $0.114\ \mathsf{kg.s^{-1}}$. Last, the rule checks if the outside temperature is higher than $0\ ^\circ\mathsf{C}$, to avoid inducing any discomfort in case of building occupation. The rule ρ_6 corresponds to a scenario where the bypass is turned on and the airflow does not increase. First sub-rule concerns the state of the bypass, second the airflow rate value and last the electrical consumption of the fan. The latter verifies its nominal operation. The rule ρ_7 occurs when the bypass is not turned on but the airflow rate is increased. The first subrule is the same rule as $\rho_{5.1}$ to detect if it is a free-cooling period. The second subrule looks at the bypass state, while the third one the airflow rate and the fan electrical power. Rule ρ_8 deals with filter fouling similarly to the one defined for winter period.

3.1.3 Maps of the system operation

After the filtering of the data using the so-called expert rules, the HASTIE algorithm is used to select $N_H = 500$ most representative points. Then, using the dimensionality reduction technique, two maps are

Table 1. *Coefficients values for the expert rules to detect fault system operation during the winter season.*

Faults	**Rule**	**Sub-rule**	**Physical quantity**	U_i	U_j	U_∞	β
Supply fan failure	ρ_1	$\rho_{1.1}$	Supply airflow rate	0	$Q_{v,sup}$	-0.036	0.01
		$\rho_{1.2}$	Supply fan electrical power	0	$P_{v,sup}$	-25	8
Exhaust fan failure	ρ_2	$\rho_{2.1}$	Exhaust airflow rate	0	$Q_{v,exh}$	-0.036	0.01
		$\rho_{2.2}$	Exhaust fan electrical power	0	$P_{v,exh}$	-25	8
Frost coil failure	ρ_3	$\rho_{3.1}$	Frost coil electrical power	0	$P_{b,fro}$	-2.5	1
		$\rho_{3.2}$	Outside air temperature	0	T_{out}	-5	1
Heat coil failure	ρ_4	$\rho_{4.1}$	Heat coil electrical power	0	$P_{b,hc}$	-2.5	1
		$\rho_{4.2}$	Supply air temperature	$T_{c,sup}$	T_{sup}	1	1
Exhaust fan belt breakdown	ρ_5	$\rho_{5.1}$	Exhaust airflow rate	0	$Q_{v,exh}$	-0.01	0.003
		$\rho_{5.2}$	Exhaust fan electrical power	$P_{v,exh}$	0	25	4
Frost coil regulation	ρ_6	$\rho_{6.1}$	Outside air temperature	0	T_{out}	-5	1
		$\rho_{6.2}$	Frost coil electrical power	$P_{b,fro}$	0	2.5	1
		$\rho_{6.3}$	Supply fan electrical power	$P_{v,sup}$	0	10	1
		$\rho_{6.4}$	pre-heating temperature time derivative	T'_{pre}	0	0	0.1
Heat coil regulation	ρ_7	$\rho_{7.1}$	Supply air temperature	$T_{c,sup}$	T_{sup}	0	1
		$\rho_{7.2}$	Heat coil electrical power	$P_{b,hc}$	0	5	1
		$\rho_{7.3}$	Supply fan electrical power	$P_{v,sup}$	0	10	1
		$\rho_{7.4}$	supply temperature time derivative	T'_{sup}	0	0	0.1
Filter fouling	ρ_8	$\rho_{8.1}$	Supply airflow rate	0	$Q_{v,sup}$	-0.036	0.015
		$\rho_{8.2}$	Supply fan electrical power	$P_{v,sup}$	0	40	2.5

constructed, one for each season. Indeed, the AHU has two different operations depending on winter and summer seasons. It permits to have a clear reading of the system operation.

The winter map obtained using the dimensionality reduction technique is illustrated in Figure 6(a). The 500 points of the operation system are represented in the map. As remarked, several clusters are identified with a major one in the middle of the map and a dozen minors around. However, this map cannot be used for fault detection. In other words, the operator cannot interpret this map since it only shows the results of the dimensionality reduction, *i.e.* points placed in a two-dimensional space. To use those results for fault detection, it is important to color the map according to the intensity of the indicator λ. It leads to Figure 6(b). This representation enables to identify the areas of faulty operation (when $\lambda > 0$), *i.e.* at least one rule is strictly higher than zero, and nominal operation (when $\lambda = 0$). One may note that the nominal operation of the system is located in the map center. Surrounding clusters corresponds to faulty system operation. Particularly, when $\lambda > 1$ it represents points of coupled faulty operation, *i.e.* two faults occur at the same time. Such faults are located on the west and southeast sides of the map. Last, another filtering is carried out by associating a color to each of the fault to produce the map in Figure 6(c). Note that the coloration is possible since the magnitude of the severity indicator of the generated data is known. It enables to provide a clear two-dimensional representation of the system operation. Each cluster with a specific color indicates a faulty case, while black points depict a nominal activity. The coupled faults have a bi- or tri-color representation and are placed at the border between the two concerned fault zones.

Results for the summer period are presented in Figure 7. As for the previous map, the methodology permits to separate several clusters each corresponding to a specific case. The nominal operation is located in the center. Each fault is associated to an area close to a peripheral area. In this modeling results, there is only one point for coupled faults based in the south region.

Table 2. *Coefficients values for the expert rules to detect fault system operation during the summer season.*

Faults	**Rule**	**Sub-rule**	**Physical quantity**	U_i	U_j	U_∞	β
Supply fan failure	ρ_1	$\rho_{1.1}$	Supply airflow rate	0	$Q_{v,sup}$	-0.03	0.01
		$\rho_{1.2}$	Supply fan electrical power	0	$P_{v,sup}$	-25	0.1
Exhaust fan failure	ρ_2	$\rho_{2.1}$	Exhaust airflow rate	0	$Q_{v,exh}$	-0.03	0.01
		$\rho_{2.2}$	Exhaust fan electrical power	0	$P_{v,exh}$	-25	0.1
Exhaust fan belt breakdown	ρ_3	$\rho_{3.1}$	Exhaust airflow rate	0	$Q_{v,exh}$	-0.01	0.001
		$\rho_{3.2}$	Exhaust fan electrical power	$P_{v,exh}$	0	35	8
Supply fan belt breakdown	ρ_4	$\rho_{4.1}$	Supply airflow rate	0	$Q_{v,sup}$	-0.01	0.001
		$\rho_{5.2}$	Supply fan electrical power	$P_{v,sup}$	0	35	8
Bypass regulation failure n°1	ρ_5	$\rho_{5.1}$	Moving average temperature	$\overline{T}_{ret}$	$\overline{T}_{out}$	2	1
		$\rho_{5.2}$	Bypass state	0	b	-1	0.1
		$\rho_{5.3}$	Moving average airflow rate	$\overline{Q}_{sup}$	0	0.114	0.001
		$\rho_{5.4}$	Outside air temperature	$\overline{T}_{out}$	0	0	0.1
Bypass regulation failure n°2	ρ_6	$\rho_{6.1}$	Bypass state	b	0	0	0.1
		$\rho_{6.2}$	Supply airflow rate	0	$Q_{v,sup}$	-0.114	0.001
		$\rho_{6.3}$	Supply fan electrical power	$P_{v,sup}$	0	2.5	1
Bypass regulation failure n°3	ρ_7	$\rho_{7.1}$	Moving average temperature	$\overline{T}_{ret}$	$\overline{T}_{out}$	2	1
		$\rho_{7.2}$	Bypass state	0	b	-1	0.3
		$\rho_{7.3}$	Moving average airflow rate	$\overline{Q}_{sup}$	0	0.055	0.001
		$\rho_{7.4}$	Supply fan electrical power	$P_{v,sup}$	0	55	1
Filter fouling	ρ_8	$\rho_{8.1}$	Supply airflow rate	0	$Q_{v,sup}$	-0.3579	0.02
		$\rho_{8.2}$	Supply fan electrical power	$P_{v,sup}$	0	150	2.5

3.2 Online phase: projection of experimental data

After the map construction, the online phase is carried out by projecting experimental data obtained in [14]. by monitoring an AHU unit. The experimental data set includes nominal and faulty operations of the system for both summer and winter periods. Before projecting the experimental data on the maps, the first step is to compute the severity indices of the rules defined in Section 3.1.2. The required parameters are gathered in Tables 1 and 2. Then severity indices are projected on the corresponding map (winter or summer) using the RBF interpolation. The issue is to validate the methodology for fault detection and diagnosis.

3.2.1 Winter map

The results are first illustrated for the winter map and the rule ρ_2 concerning the exhaust fan failure. Figure 8(a) shows the time evolution of the exhaust fan airflow and power consumption. As remarked, for $t > 0$, both airflow and power consumption decrease to zero. Accordingly, the severity index drops from 0 to 1 in Figure 8(b). It highlights a failure of the exhaust fan since it does not operate in nominal condition. The severity index σ_2 is projected on the winter map in Figure 8(c). As the index is negative, the projected points remain in the nominal area. When the indicator becomes positive, the points move toward the orange North-West area of the map. This area corresponds to the exhaust fan fault. Thus, a precise diagnosis of the appearing fault is done.

The reliability of the approach is also shown for the rule regarding the heat coil failure. Figure 9(a) gives the heat coil power consumption together with the supply air temperature and the set-point heat coil

temperature. When $t < 0$, the heat coil is operating with a power consumption around 600 W. At $t = 0$, the coil fails and its power consumption vanishes. At the same time, the supply air temperature starts to decrease, becoming lower than the heat coil set-point temperature of 26 °C. At this time, the failure of the system is stated and the severity index reaches 1 as remarked in Figure 9(b). The results of the index projection on the winter map are shown in Figure 9. When the severity index is positive, the projected data are located in the correct fault area.

Three other faults have been generated experimentally for the winter season: the supply fan failure (ρ_1), the frost coil failure (ρ_3) and the exhaust fan belt breakdown (ρ_5). Figure 10 presents the results of the projection. For the three faults, the data are first located in the nominal area and progressively slide to the corresponding fault area. Thus, the diagnosis of the failure is carried out with accuracy.

3.2.2 Summer map

An illustration of the process is shown in Figure 11. For the sake of compactness, the figures are presented for a time horizon of 6 minutes where $t = 0$ corresponds to the appearance of the fault. Figure 11(a) shows the concerned measurements of the supply air fan flow rate and power consumption that enable to detect the fan failure. Both measurements start decreasing at $t = 0$ indicating a failure of the supply fan. By filtering this data using the expert rules ρ_1, the severity index is computed and presented in Figure 11(b). By definition, the index is lower than 0 in case of nominal operation. The index grows as the fault appears to reach almost 1 when the fan failure is established. The data of the severity index are projected on the so-called summer map in Figure 11(c). The first data, when $t < 0$, are located in the nominal operation (black zone). Then, when $t > 0$ and $\sigma > 1$, the data are projected into the red zone, corresponding to a supply failure fault. Thus, the methodology enables to project the experimental data into the correct zone to permit a fast and accurate fault detection and diagnosis.

Another demonstration of the validity of the methodology is proposed for the rule ρ_7, in Figure 12. This fault is detected by 4 sub-rules. The first one detects a free-cooling period since the outside temperature is lower (around 15 °C) than the inside one (around 24 °C). The next sub-rules observes that the bypass is not turned on since the b remains null for the whole sequence. However, it can be remarked with the airflow rate and fan electrical power increases for $t > 0$. This bypass regulation failure is highlighted with the severity index reaching 1 as shown in Figure 12(b). The projection of the severity index on the data permits to detect the fault. The index is first projected on a nominal operation region and then on the bypass regulation fault 3.

The efficiency of the methodology has been verified for four other faults of the summer period using experimental data. Results of the projection are given in Figure 13. The projection of the severity index systematically corresponds to the correct region (nominal or fault) allowing a clear, intuitive and fast diagnosis of the fault. Note that in Figure 13(d), the approach enables to detect a slow degradation of the system regarding the bypass regulation fault ρ_2. There is a slow transition between black (nominal operation to green (bypass fault 1) and finally light blue (bypass fault 2)).

3.3 Complementary remarks

The reliability of the method to carry out fault and detection diagnosis has been demonstrated using experimental results. Some complementary remarks can be noted. One may notice some differences between the summer and winter operation map of the system in Figures 6(c) and 7. Particularly, the winter map is more detailed with spread areas. On the contrary, the summer map is less exhaustive. For instance, the supply and exhaust fan faults are represented by one singular points. This lack of details is a consequence of the offline phase and the generation of numerical results. The model does not enable to generate values of some severity indicators with smooth transition between -1 and 1. Some improvements of the simulation programs are required to better refine the indicator space. Given the results from [28], the use of experimental data may lead to more refined maps. In the context of real building operation, one can build a first map using a simulation program. After the first monitoring season, a possibility to explore is to re-generate the map using a combined numerical and obtained experimental data.

The computational burden of the method arises from the algorithm used for dimensionality reduction during the offline phase to create the map. The complexity of the algorithm scales with $\mathcal{O}(N^2)$, where N is the total number of data generated using the building simulation programs. In our case N scales with $\mathcal{O}(10^5)$ ($N_m = 12$ measurements generated for a time grid of $N_t = 70080$ points) so the complexity of the algorithm is very high. For this reason the number of data is reduced to $N_H = 500$ using the HASTIE algorithm. The latter enables to select the most representative points outs. For the winter and summer map, 10 clusters are expected (8 to 9 faults plus nominal state). Thus, $N_H = 500$ corresponds roughly to 50 points to represent each cluster, which is a satisfying number for the representation of the system operation. Furthermore, parametric studies for different value of N_H highlights that it corresponds to a good compromise between computational cost and accuracy of the map. Note that for this value, the map construction requires 3 min on a normal laptop.

After the offline phase, a map of the system operation is generated. As presented in Figures 6(c) and 7 some regions are highlighted for nominal and faulty operations. The nominal operation is located in the center while the faulty configurations are around. For the moment, the fault detection is based on the position of the measured data projection compared to the identified areas. However, it could be possible to detect the fault according to the euclidean distance on the map between the nominal region (*i.e.* the center of the circle) and the position of the projection. For each faulty region, a threshold could be defined.

Note that the fault detection is almost immediate. As soon as the experimental data of the building energy management system are recorded, the computation of the severity indexes and their projection on the map are very fast on a normal-cost laptop equipped with an Intel Core i5 processor and 12GB RAM. Actually, the detection depends on the monitoring time step of the building energy management system and the transition between nominal and faulty operations. In Figures 11(b), 8(b), 9(b) and 12(b), the transition between nominal and faulty operations scales with one minute as the fault detection.

4 Conclusion

Within the environmental issues, fault diagnosis methods are of major importance to detect HVAC system failures. It enables to avoid excessive consumption and improve occupants comfort. Within this context, an innovative FDD approach is presented based on a two phase procedure. The first phase is realized before the diagnosis. It aims at elaborating a map of the system operations with distinct areas. Each area corresponds to the nominal operation or to a specific system faults. The map is built using a dataset of both nominal and faulty states. The dataset can originate from time varying experimental measurement and/or numerical results. The dataset are then filtered according to expert rules to construct a set of severity indicators. The results are subsequently treated using a dimension reduction method to approximate the data structure by a low dimensional representation of a subset of the points, corresponding to the map of the system operation. Note that the analyze *per se* of the experts rules could be sufficient to detect faulting operations. However, as mentioned in [10], the interpretability of faults by operations staff is an important limitation. FDD tools based on experts rules generate some alarms without including operators to address them. The energy management systems fail in consolidating the data into a clear and understandable format [12, 13]. Therefore, the proposed FDD tool combined the experts rules analysis with a data-driven approach which enables to produce *one* map of the system. It provides a synthesis of the nominal and faulty operations. This representation is easily understandable by operators to engage solutions. The second phase of the FDD method is online, *i.e.* it occurs during the monitoring by the building energy management system. It aims at detecting the faults. The measured data are filtered following the same expert rules to compute the severity indices. Those indices are then projected *a posteriori* on the maps built during the preliminary phase using radial basis function interpolation. The projection enables to locate the actual state of the system in the map, namely in a nominal or faulty region.

The reliability of this method has been evaluated for a AHU unit that could be used in a small office or house. The maps are generated using numerical results from the EnergyPlus program. Faulty and nominal operation of the system has been modeled to generate a total of $12 \times 70\,080$ data. Then, eight expert rules have been defined for both winter and summer season. The failures concern the supply and exhaust fans,

the heat and frost coils, the belt breakdown, the coils and bypass regulations and the filter fouling. Then, each set of eight severity indices is approximated by a reduced dimension space. It permits to elaborate two maps (one for each season) of the system operation. Each map has a nominal operation area in the middle and eight faulty region in the peripheral region. The region are well separated and coupled faults are also correctly highlighted. This first phase enables to produce a clear and understandable representation of the system operation. Then, the accuracy of the fault detection is evaluated using experimental data generated in previous work [14]. Those data have been obtained through an experimental campaign representative of a monitoring by a building energy management. Each experimental data are filtered according to the expert rules and then projected on each map. For each of eleven faults, the method projects the new data into the correct area. If the system operates in a nominal state, then the data are projected into the middle zone. Respectively, if the system has a fault, the data are projected in the corresponding fault area. Therefore, the reliability of the method to detect and diagnose the faults is verified.

Future works should focus on evaluating the approach with more complex experimental data obtained from a real building monitoring system. Particularly, the efficiency of the approach should be evaluated to detect slow degradation of HVAC system.

Nomenclature

Latin letters

Symbols	Description	Units
P	Power	$[\mathsf{W}]$
Q	airflow	$[\mathsf{kg\,.\,s^{-1}}]$
T	Temperature	$[\,^{\circ}\mathsf{C}]$
t	Time	$[\mathsf{s}]$

Abbreviation

Symbols	Description
$Exh.$	In the exhaust duct
$fro.$	frost coil
$hc.$	heat coil
$Nom.$	At the nominal value
$Out.$	At the outdoor air location
$Ret.$	At the return air location
$Sup.$	In the supply duct

Acknowledgements

The authors acknowledge the laboratory LOCIE for the funding through the “AAP interne”. This project is supported by the Interreg V France-Switzerland European Territorial Cooperation Program and has benefited from a European grant of 607 . 776, 49 € through the European Regional Development Fund (ERDF) as well as federal funds Interreg Switzerland for 150001 CHF and 123 . 999 CHF for cantonal and communal aid.

References

[1] US Department of Energy. *Buildings Energy Data Book*. 2012. 1

[2] U.S. Energy Information Administration (EIA). Energy Consumption by Sector. Technical report. 1

[3] Fu Xiao and Shengwei Wang. Progress and methodologies of lifecycle commissioning of HVAC systems to enhance building sustainability. *Renewable and Sustainable Energy Reviews*, 13(5):1144–1149, June 2009. 1

[4] Peter Warburton, K. J. Butcher, and Chartered Institution of Building Services Engineers, editors. *Building Control Systems*. CIBSE Guide H. CIBSE, London, 2. ed edition, 2009. 1

[5] Venkat Venkatasubramanian, Raghunathan Rengaswamy, Kewen Yin, and Surya N Ka. A review of process fault detection and diagnosis Part I: Quantitative model-based methods. *Computers and Chemical Engineering*, page 19, 2003. 1

[6] Ken Bruton, Paul Raftery, Barry Kennedy, Marcus M. Keane, and D. T. J. O'Sullivan. Review of automated fault detection and diagnostic tools in air handling units. *Energy Efficiency*, 7(2):335–351, 2014. 1

[7] Woohyun Kim and Srinivas Katipamula. A review of fault detection and diagnostics methods for building systems. *Science and Technology for the Built Environment*, 24(1):3–21, 2018.

[8] Yuebin Yu, Denchai Woradechjumroen, and Daihong Yu. A Review of Fault Detection and Diagnosis Methodologies on Air-Handling Units. *Energy and Buildings*, 82:550–562, 2014. 1

[9] Juhani Hyvarinen, J.C. Visier, M. Stilianou, H. Yoshida, K. Sagara, and et.al. Annex 25 : Real Time Simulation of HVAC Systems for Building Optimisation, Fault Detection and Diagnostics. Technical report, 1999. 2

[10] H. Burak Gunay and Zixiao Shi. Cluster analysis-based anomaly detection in building automation systems. *Energy and Buildings*, 228:110445, 2020. 2, 14

[11] Sanja Lazarova-Molnar, Hamid Reza Shaker, Nader Mohamed, and Bo Norregaard Jorgensen. Fault Detection and Diagnosis for Smart Buildings: State of the Art, Trends and Challenges. In *2016 3rd MEC International Conference on Big Data and Smart City (ICBDSC)*, pages 1–7, Muscat, 2016. IEEE. 2

[12] K. Bruton, P. Raftery, P. O'Donovan, N. Aughney, M. M. Keane, and D.T.J. O'Sullivan. Development and alpha testing of a cloud based automated fault detection and diagnosis tool for air handling units. *Automation in Construction*, 39:70–83, 2014. 2, 14

[13] Z. Shi and W. O'Brien. Development and implementation of automated fault detection and diagnostics for building systems: A review. *Automation in Construction*, 104:215–229, 2019. 2, 14

[14] Hugo Geffroy, Julien Berger, Evelyne Gonze, and Catherine Buhe. Experimental dataset of an ahu air-to-air heat exchanger with normal and emulated fault operations. *under submission*, pages 1–30, 2021. 2, 8, 12, 15

[15] Trevor Hastie, Robert Tibshirani, and J. H. Friedman. *The Elements of Statistical Learning: Data Mining, Inference, and Prediction*. Springer series in statistics. Springer, New York, NY, 2nd edition, 2009. 4, 5

[16] L. Cayton. Algorithms for manifold learning. *Univ. of California at San Diego Tech. Rep*, 2005. 4

[17] Warren S. Torgerson. Multidimensional Scaling: I. Theory and Method. *Psychometrika*, 17(4):401–419, 1952. 4

[18] G. Hinton and S. Roweis. Stochastic neighbor embedding. In *Proceedings of the 15th International Conference on Neural Information Processing Systems*, NIPS'02, page 857–864, Cambridge, MA, USA, 2002. MIT Press. 4, 6

[19] Laurens van der Maaten and Geoffrey Hinton. Visualizing data using t-sne. *Journal of Machine Learning Research*, 9(86):2579–2605, 2008. 4

[20] Jarkko Venna, Jaakko Peltonen, Kristian Nybo, Helena Aidos, and Samuel Kaski. Information retrieval perspective to nonlinear dimensionality reduction for data visualization. *Journal of Machine Learning Research*, 11(13):451–490, 2010. 4

[21] J. A. Lee, E. Renard, G. Bernard, P. Dupont, and M. Verleysen. Type 1 and 2 mixtures of kullback–leibler divergences as cost functions in dimensionality reduction based on similarity preservation. *Neurocomputing*, 112:92–108, 2013. Advances in artificial neural networks, machine learning, and computational intelligence. 4

[22] S. L. France and J. D. Carroll. Two-way multidimensional scaling: A review. *IEEE Transactions on Systems, Man, and Cybernetics, Part C (Applications and Reviews)*, 41(5):644–661, 2011. 4

[23] https://scikit-learn.org/stable/auto_examples/manifold/plot_compare_methods.html. consulted February 2022. 5

[24] S. Lespinats, B. Colange, and D. Dutykh. *Data Science Context*, pages 1–30. Springer International Publishing, 2022. 4, 7

[25] F. Pedregosa, G. Varoquaux, A. Gramfort, V. Michel, B. Thirion, O. Grisel, M. Blondel, P. Prettenhofer, R. Weiss, V. Dubourg, J. Vanderplas, A. Passos, D. Cournapeau, M. Brucher, M. Perrot, and E. Duchesnay. Scikit-learn: Machine learning in Python. *Journal of Machine Learning Research*, 12:2825–2830, 2011. 6

[26] B. Colange. Adaptive student kernel imbedding (aski) for dimensionality reduction [source code] https://doi.org/10.24433/CO.4712556.v1. 2022. 7

[27] S. N. Lophaven, H. B. Nielsen, and J. Sondergaard. Dace a matlab krigging toolbox version 2.0 https://www.omicron.dk/dace.html. *IMM INFORMATICS AND MATHEMATICAL MODELLING, Technical University of Denmark*, 2002. 7

[28] H. Geffroy, J. Berger, B. Colange, S. Lespinats, Denys D. Dutykh, G. Sauce, and C. Buhe. Use of multidimensional scaling for fault detection or monitoring support in a continuous commissioning. *Proceedings of the 16th IBPSA Conference, IBPSA*, Rome, Italy:877–884, 2019. 13

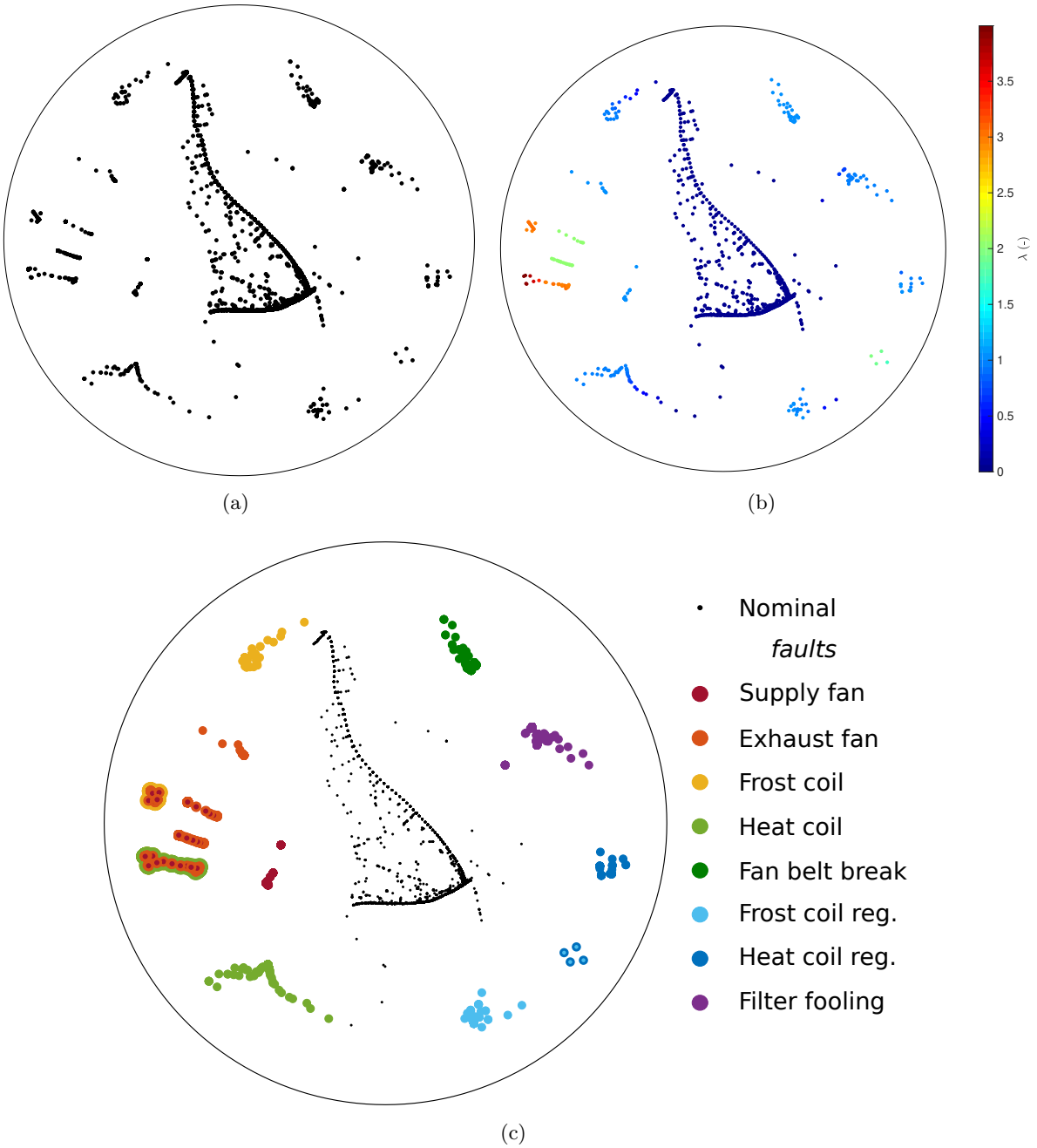

Figure 6. *Map of the system operation for winter:* (a) *results of the dimensionality reduction,* (b) *display of total severity* λ *and* (c) *fault type representation.*

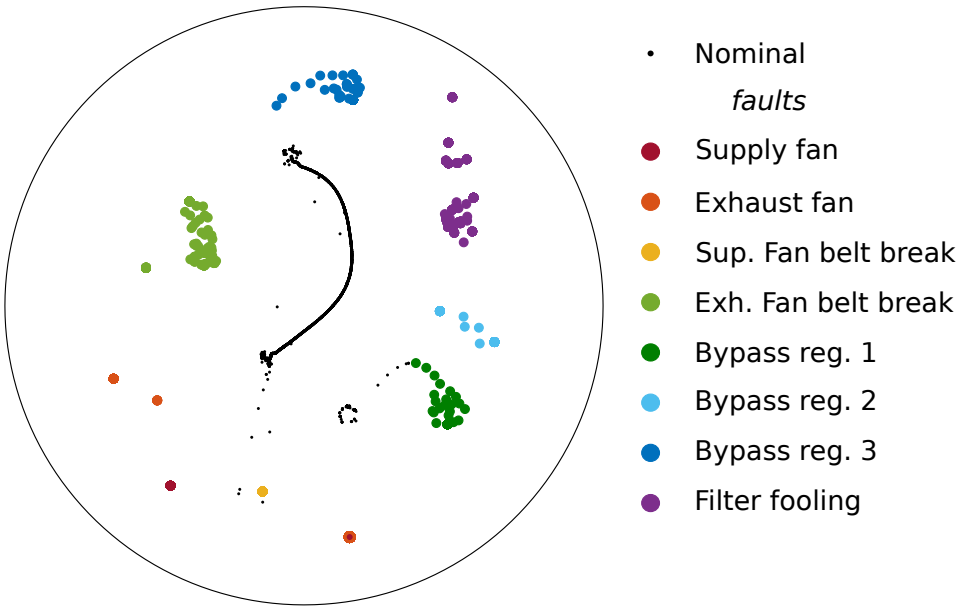

Figure 7. *Map of the system operation for summer: final representation.*

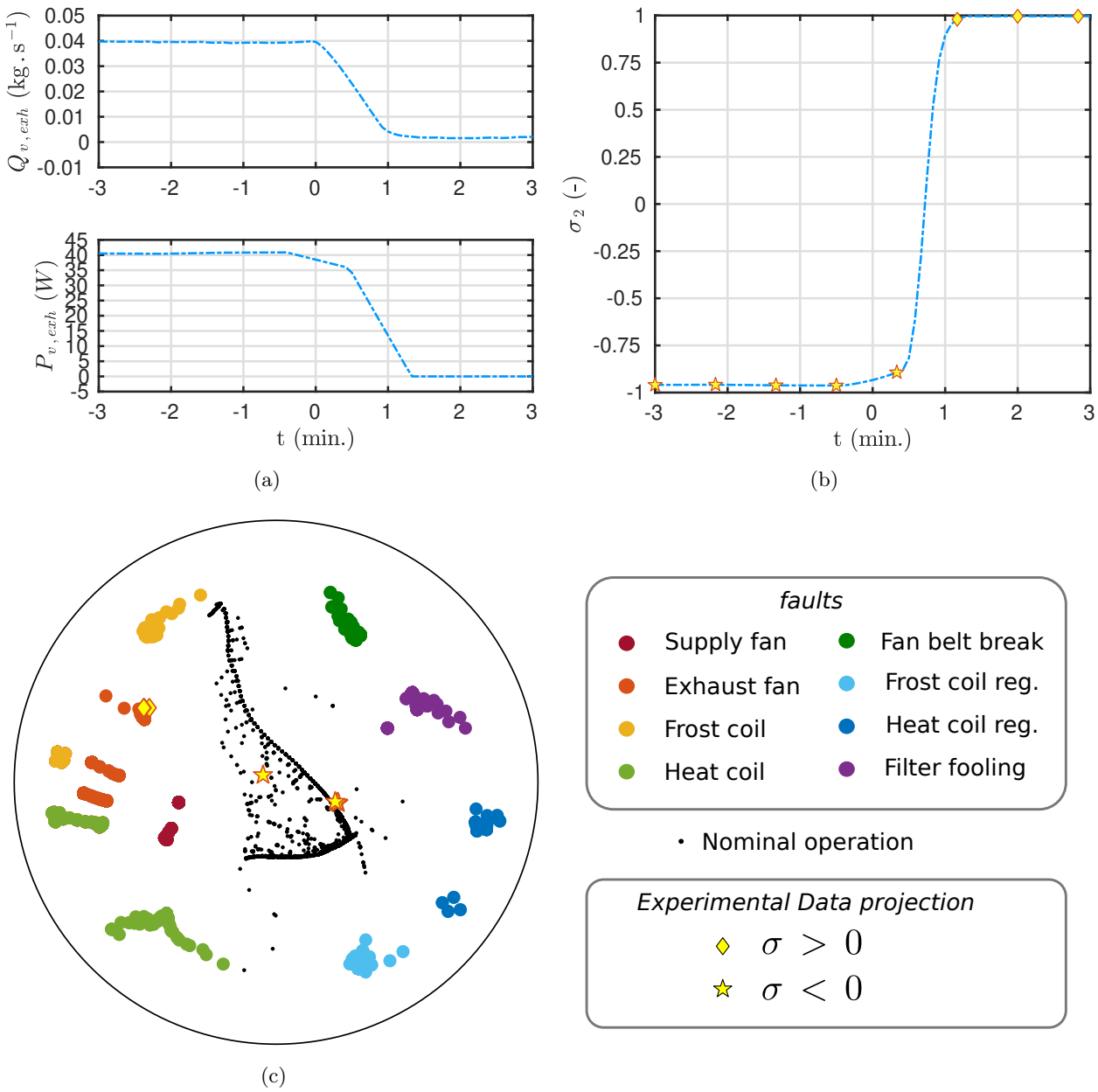

Figure 8. *Experimental data obtained during the winter campaign: exhaust fan airflow and power consumption* (a). *Computed severity index according to the expert rules* (b). *Projection of the experimental data on the winter map for fault detection of exhaust air fan failure* (ρ_2).

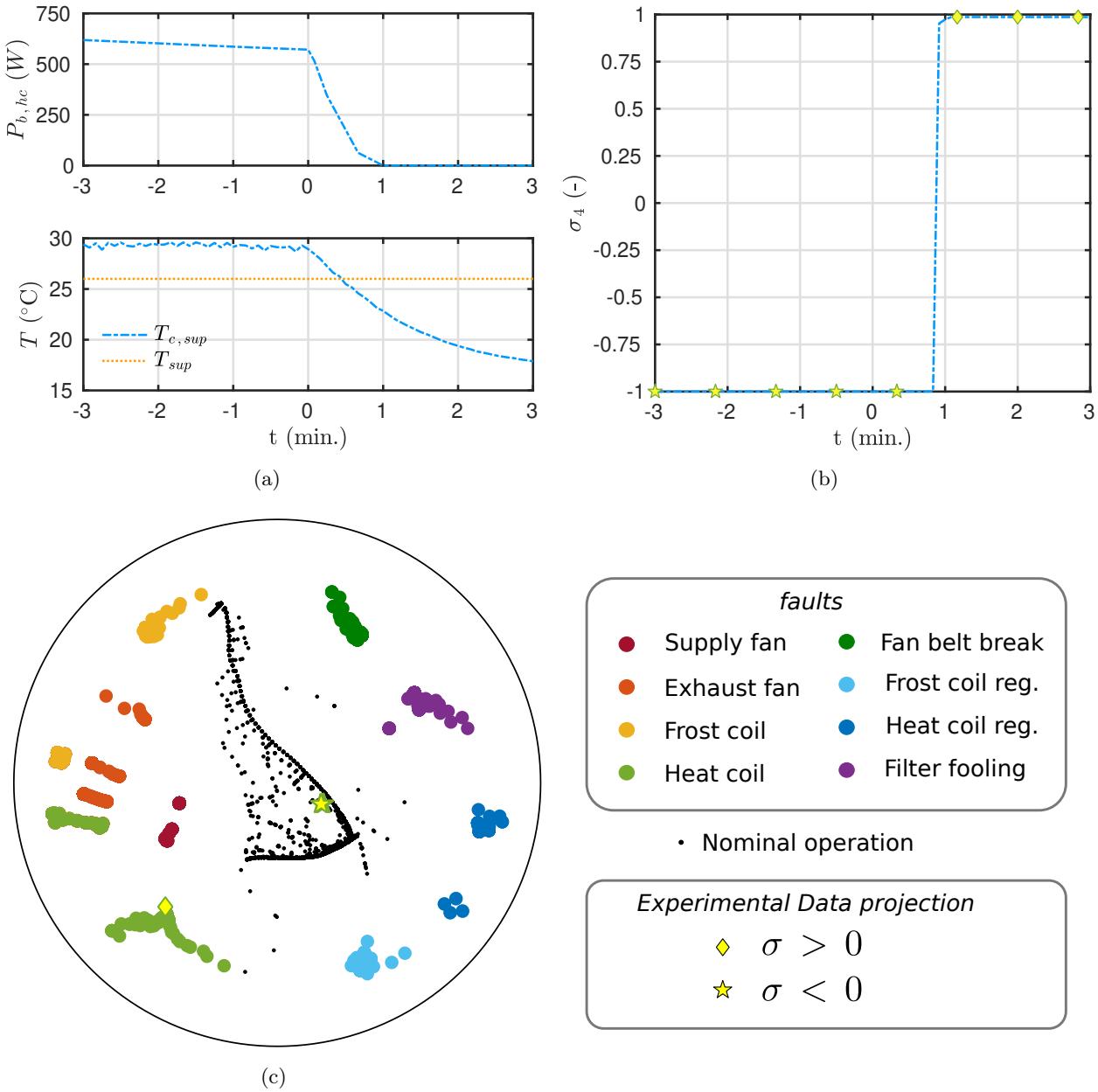

Figure 9. *Experimental data obtained during the winter campaign: heat coil power and supply air temperature* (a). *Computed severity index according to the expert rules* (b). *Projection of the experimental data on the winter map for fault detection of heat coil failure* (ρ_4).

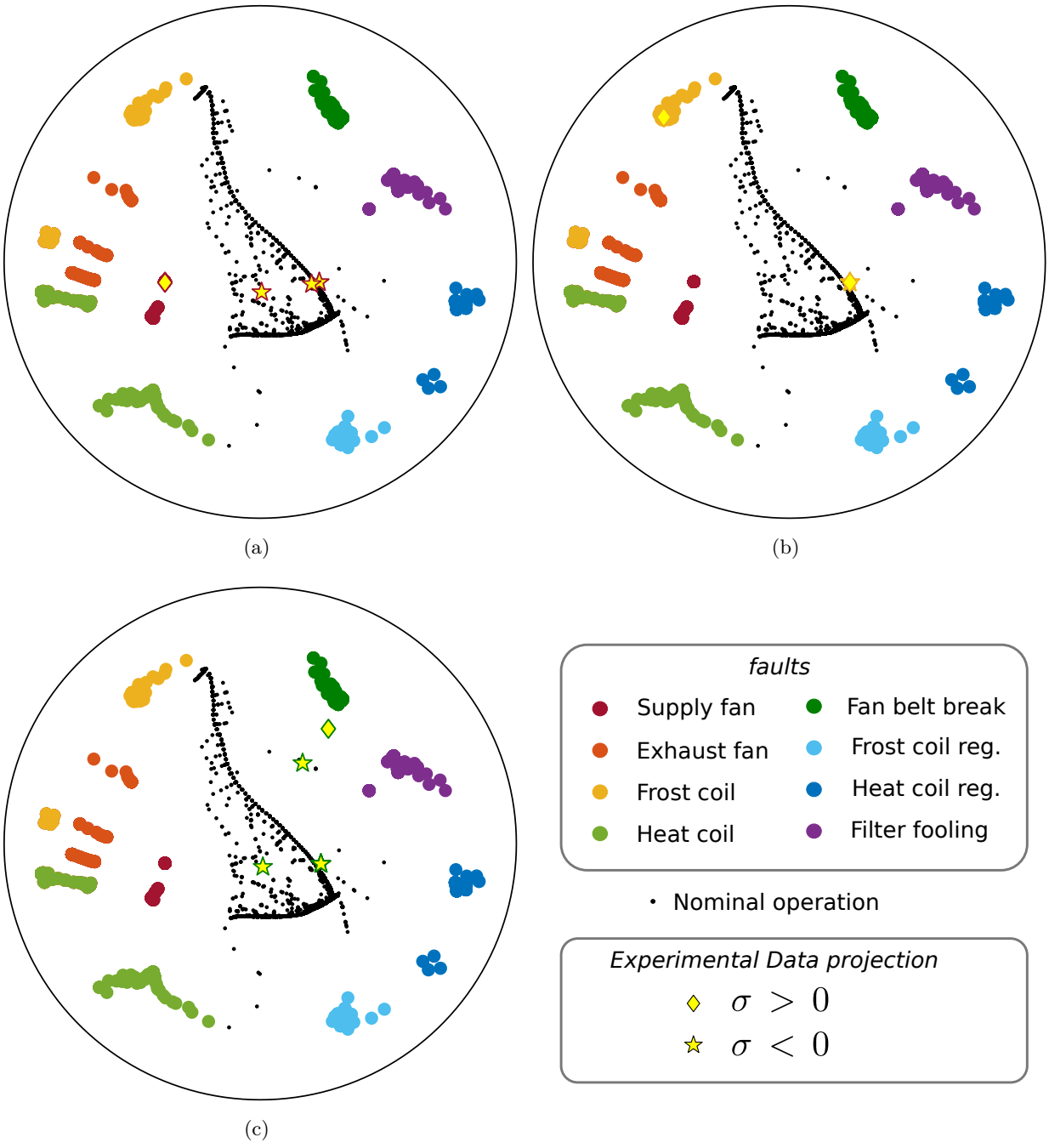

Figure 10. *Results of the projection of the experimental data on the winter map for the supply fan failure (ρ_1)* (a)*, frost coil failure (ρ_3)* (b) *and exhaust fan belt breakdown (ρ_5)* (c).

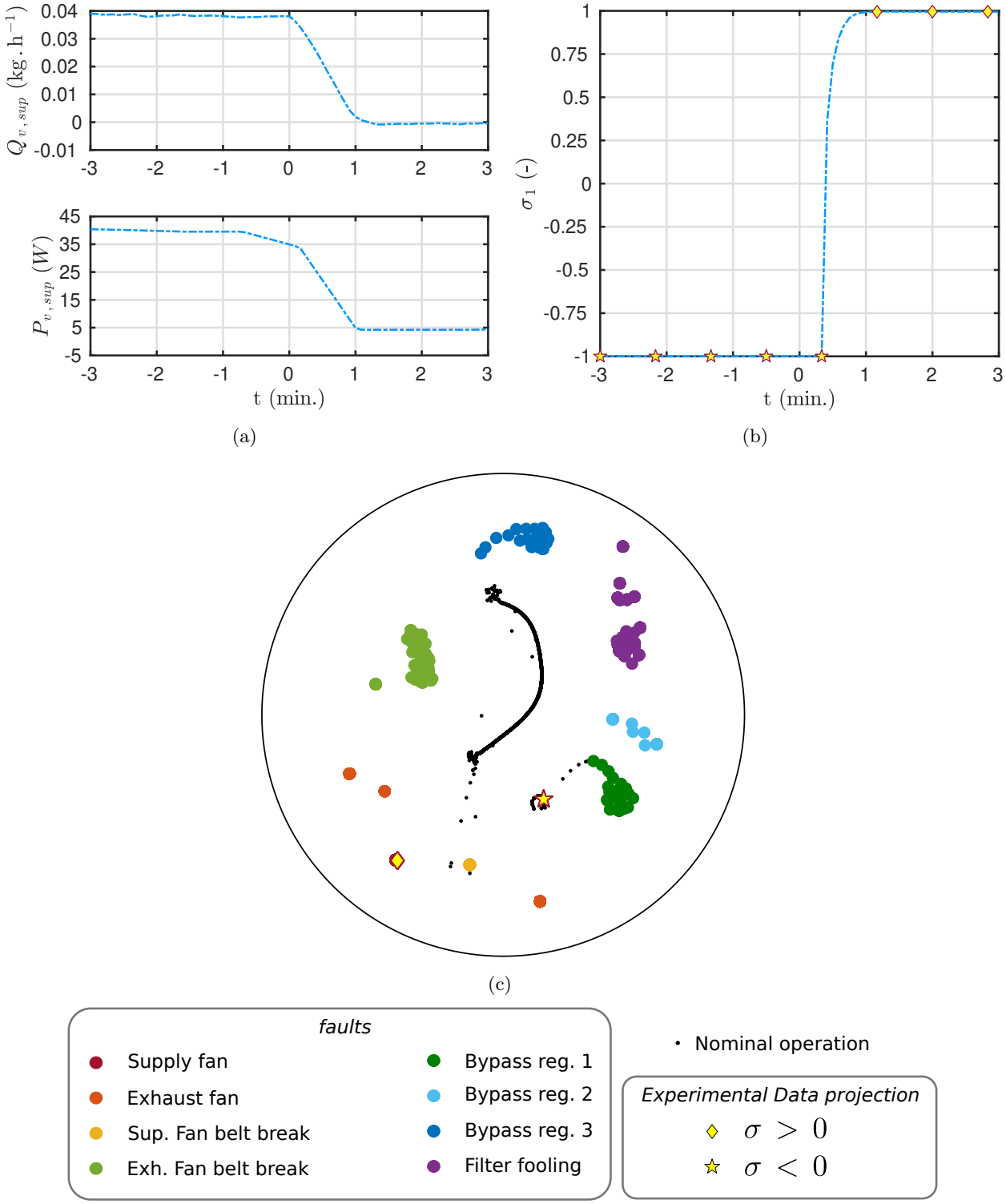

Figure 11. *Experimental data obtained during the summer campaign: supply fan airflow and power consumption* (a). *Computed severity index according to the expert rules* (b). *Projection of the experimental data on the summer map for fault detection of supply air fan failure* (ρ_1).

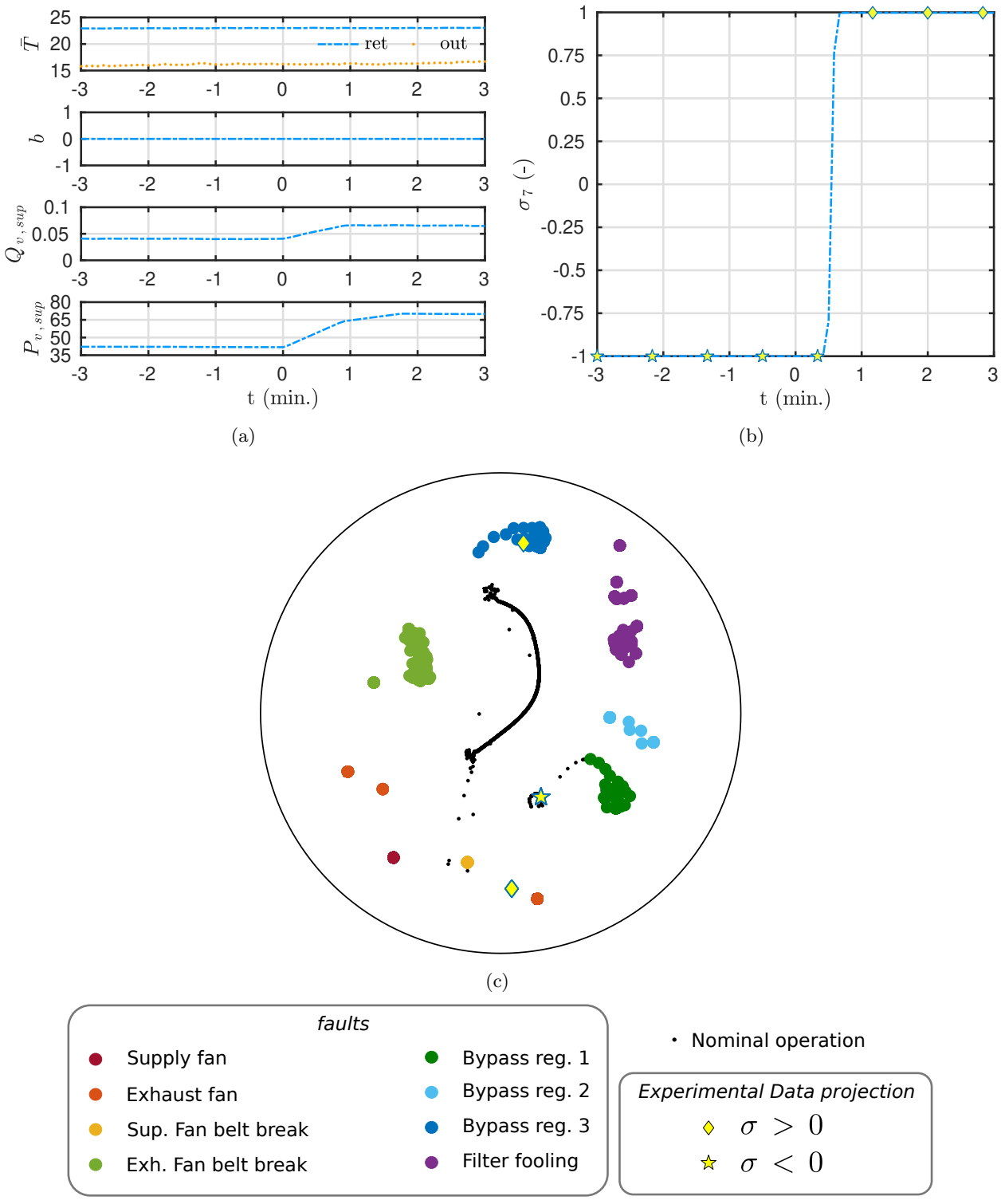

Figure 12. *Experimental data obtained during the summer campaign: moving average temperatures, bypass state, supply fan airflow and power consumption* (a). *Computed severity index according to the expert rules* (b). *Projection of the experimental data on the summer map for fault detection of bypass regulation n°3 (ρ_7).*

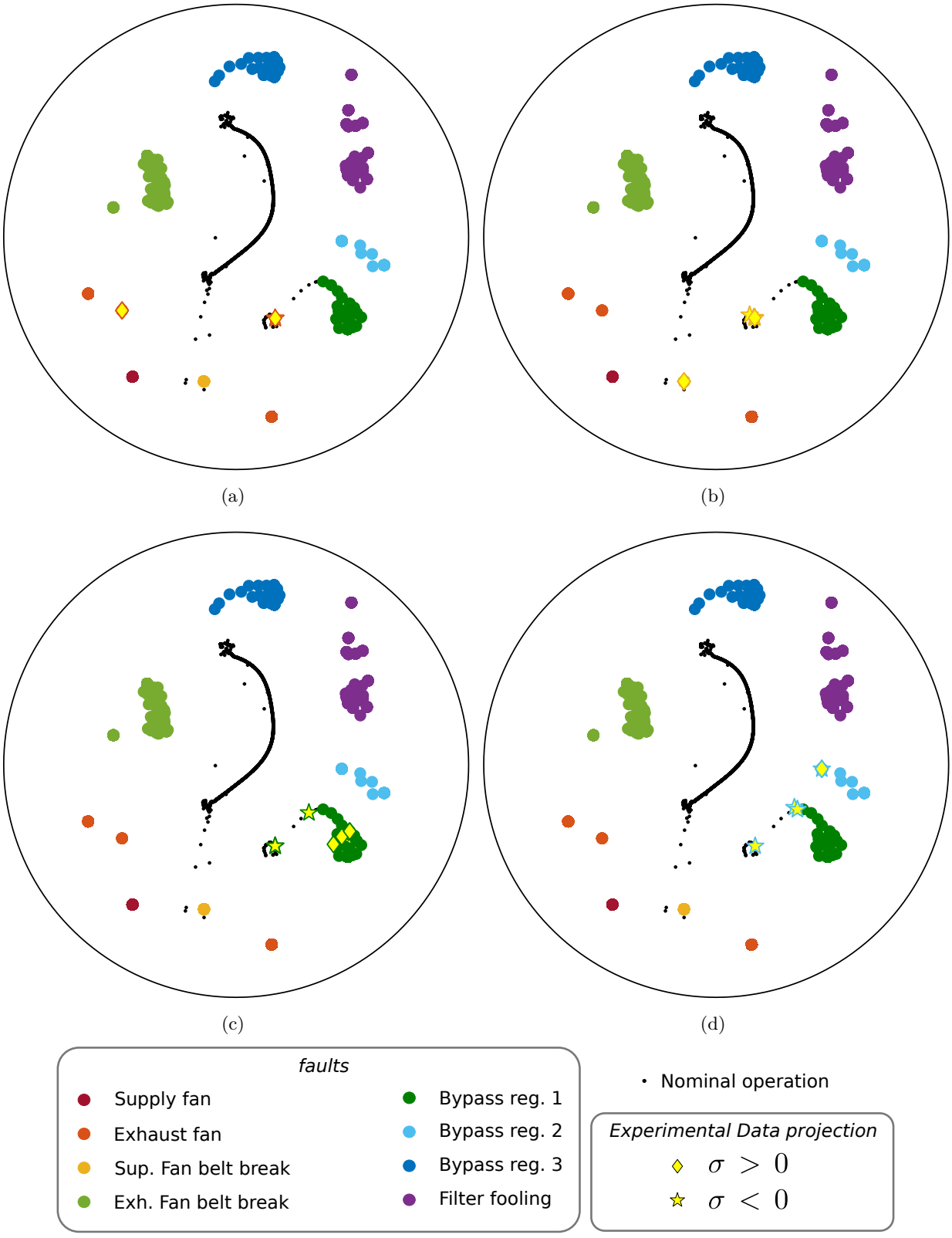

Figure 13. *Results of the projection of the experimental data on the summer map for the exhaust fan failure (ρ_2)* (a)*, exhaust fan belt breakdown (ρ_3)* (b)*, bypass regulation failure n°1 (ρ_5)* (c) *and bypass regulation failure n°2 (ρ_6)* (d)*.*